The Astrophysical Journal, 701:1804–1813, 2009 August 20 doi:10.1088/0004-637X/701/2/1804

FIVE-YEAR *WILKINSON MICROWAVE ANISOTROPY PROBE* (*WMAP**) OBSERVATIONS: BAYESIAN ESTIMATION OF COSMIC MICROWAVE BACKGROUND POLARIZATION MAPS

J. Dunkley[1,2,3], D. N. Spergel[2,4], E. Komatsu[5], G. Hinshaw[6], D. Larson[7], M. R. Nolta[8], N. Odegard[9], L. Page[1], C. L. Bennett[7], B. Gold[7], R. S. Hill[9], N. Jarosik[1], J. L. Weiland[9], M. Halpern[10], A. Kogut[6], M. Limon[11], S. S. Meyer[12], G. S. Tucker[13], E. Wollack[6], and E. L. Wright[14]

[1] Department of Physics, Jadwin Hall, Princeton University, Princeton, NJ 08544-0708, USA; j.dunkley@physics.ox.ac.uk
[2] Department of Astrophysical Sciences, Peyton Hall, Princeton University, Princeton, NJ 08544-1001, USA
[3] Astrophysics, University of Oxford, Keble Road, Oxford OX1 3RH, UK
[4] Princeton Center for Theoretical Physics, Princeton University, Princeton, NJ 08544, USA
[5] University of Texas, Austin, Department of Astronomy, 2511 Speedway, RLM 15.306, Austin, TX 78712, USA
[6] Code 665, NASA/Goddard Space Flight Center, Greenbelt, MD 20771, USA
[7] Department of Physics & Astronomy, The Johns Hopkins University, 3400 N. Charles Street, Baltimore, MD 21218-2686, USA
[8] Canadian Institute for Theoretical Astrophysics, 60 St. George Street, University of Toronto, Toronto, ON M5S 3H8, Canada
[9] Adnet Systems, Inc., 7515 Mission Dr., Suite A1C1 Lanham, MD 20706, USA
[10] Department of Physics and Astronomy, University of British Columbia, Vancouver, BC V6T 1Z1, Canada
[11] Columbia Astrophysics Laboratory, 550 W. 120th Street, Mail Code 5247, New York, NY 10027-6902, USA
[12] Departments of Astrophysics and Physics, KICP and EFI, University of Chicago, Chicago, IL 60637, USA
[13] Department of Physics, Brown University, 182 Hope St., Providence, RI 02912-1843, USA
[14] PAB 3-909, UCLA Physics & Astronomy, P.O. Box 951547, Los Angeles, CA 90095-1547, USA
Received 2008 November 26; accepted 2009 June 22; published 2009 August 6

ABSTRACT

We describe a sampling method to estimate the polarized cosmic microwave background (CMB) signal from observed maps of the sky. We use a Metropolis-within-Gibbs algorithm to estimate the polarized CMB map, containing Q and U Stokes parameters at each pixel, and its covariance matrix. These can be used as inputs for cosmological analyses. The polarized sky signal is parameterized as the sum of three components: CMB, synchrotron emission, and thermal dust emission. The polarized Galactic components are modeled with spatially varying power-law spectral indices for the synchrotron, and a fixed power law for the dust, and their component maps are estimated as by-products. We apply the method to simulated low-resolution maps with pixels of side 7.2 deg, using diagonal and full noise realizations drawn from the *WMAP* noise matrices. The CMB maps are recovered with goodness of fit consistent with errors. Computing the likelihood of the E-mode power in the maps as a function of optical depth to reionization, τ, for fixed temperature anisotropy power, we recover $\tau = 0.091 \pm 0.019$ for a simulation with input $\tau = 0.1$, and mean $\tau = 0.098$ averaged over 10 simulations. A "null" simulation with no polarized CMB signal has maximum likelihood consistent with $\tau = 0$. The method is applied to the five-year *WMAP* data, using the K, Ka, Q, and V channels. We find $\tau = 0.090 \pm 0.019$, compared to $\tau = 0.086 \pm 0.016$ from the template-cleaned maps used in the primary *WMAP* analysis. The synchrotron spectral index, β, averaged over high signal-to-noise pixels with standard deviation $\sigma(\beta) < 0.25$, but excluding $\sim$6% of the sky masked in the Galactic plane, is -3.03 ± 0.04. This estimate does not vary significantly with Galactic latitude, although includes an informative prior.

Key words: cosmic microwave background – cosmology: observations – methods: statistical – polarization – radio continuum: ISM

1. INTRODUCTION

The *Wilkinson Microwave Anisotropy Probe* (*WMAP*) has mapped the sky in five frequency bands between 23 and 94 GHz. Measurements of the temperature anisotropy in the cosmic microwave background (CMB) have led to the establishment of the ΛCDM cosmological model. Anisotropies in the CMB polarization at large scales inform us about the ionization history of the universe, allow us to probe a possible signal from gravitational waves seeded early in the universe, and lead to improved constraints on cosmological parameters when combined with temperature measurements. The three-year *WMAP* observations (Page et al. 2007) showed that polarized diffuse emission from our Galaxy dominates the primordial signal over much of the sky, making accurate estimation of the CMB signal at large angular scales challenging.

In this paper, we describe a Bayesian framework for estimating the low-resolution polarized CMB maps, and errors marginalized over possible Galactic emission. The goal of this approach is to determine not only the "best" estimate of the microwave background polarization fluctuations but to determine the uncertainties associated with foreground removal. A similar technique has also been developed by Eriksen et al. (2006, 2007) for estimating intensity maps, and has been applied to the three-year *WMAP* temperature maps. This work complements the primary analysis of the five-year *WMAP* polarization maps described in Gold et al. (2009), which uses template cleaning to estimate the CMB polarization maps. The basic five-year *WMAP* results are summarized in Hinshaw et al. (2009). This paper is structured as follows. In Section 2, we describe the sampling method used to estimate polarized maps. In Section 3, we apply it to simulated maps, and in Section 4 to the *WMAP* data. We conclude in Section 5.

* *WMAP* is the result of a partnership between Princeton University and NASA's Goddard Space Flight Center. Scientific guidance is provided by the *WMAP* Science Team.

2. ESTIMATION OF POLARIZATION MAPS

The large-scale polarized radiation observed by *WMAP* is the sum of at least three components: the primordial CMB, synchrotron emission, and thermal dust emission. Here, we briefly review the Galactic emission mechanisms, for more details see, e.g., Page et al. (2007). Both synchrotron and thermal dust emission are polarized due to the Galactic magnetic field, measured to have a coherent spiral structure parallel to the Galactic plane, as well as a significant turbulent component (Spitzer 1998; Beck 2001; Vallée 2005; Han 2006). The effective strength of the field is of the order of ~ 10 μG, thought to be split roughly equally between the coherent and turbulent components (Crutcher et al. 2003). Synchrotron emission is produced by relativistic cosmic-ray electrons accelerated in this magnetic field (see Strong et al. 2007 for a review of cosmic ray propagation). For electrons with a power-law distribution of energies

$$N(E) \propto E^{-p}, \tag{1}$$

the frequency dependence of the emission is characterized by antenna temperature $T(\nu) \propto \nu^{\beta}$ with spectral index $\beta = -(p+3)/2$, with typically $\beta \sim -3$ (Rybicki & Lightman 1979). However, since synchrotron loss is proportional to E^2, older sources of electrons should have a lower energy distribution and a steeper spectral index of synchrotron emission, compared to regions of recently injected electrons. This leads to a synchrotron index that varies over the sky (Lawson et al. 1987; Reich & Reich 1988) and is expected to steepen away from the Galactic plane (Strong et al. 2007), with evidence of this behavior seen in the *WMAP* data (Bennett et al. 2003). Since the cosmic-ray electrons emit radiation almost perpendicular to the Galactic magnetic field in which they orbit, they can produce polarization fractions as high as $\sim$75% (Rybicki & Lightman 1979), although integration of multiple field directions along a line of sight reduces this level. The fractional polarization observed at radio frequencies in the range 408 MHz to 2.4 GHz is further lowered due to Faraday rotation (Duncan et al. 1995; Uyaniker et al. 1999; Wolleben et al. 2006). In the WMAP 23 GHz data, the polarization fraction is as high as 50% on significant portions of the sky (Kogut et al. 2007).

Thermal dust intensity has been well measured by the *IRAS* and *COBE* missions and extrapolated to microwave frequencies by Finkbeiner et al. (1999). Polarization arises since grains tend to align their long axes perpendicular to the Galactic magnetic field via, for example, the Davis–Greenstein mechanism (Davis & Greenstein 1951), and depending on their composition can be polarized up to a modeled maximum of $\sim$20% parallel to the long axes (e.g., Hildebrand & Dragovan 1995; Draine & Fraisse 2009). Observations of starlight, polarized perpendicular to the dust grains, are consistent with this picture (Heiles 2000; Berdyugin et al. 2001), as are the three-year *WMAP* observations (Page et al. 2007; Kogut et al. 2007). A population of smaller spinning dust grains formed of polycyclic aromatic hydrocarbons may also emit a significant amount of microwave radiation due to electric dipole rotational emission (Draine & Lazarian 1999; Draine & Li 2007). This question is discussed in, e.g., Hinshaw et al. (2007), Dobler & Finkbeiner (2008), and Gold et al. (2009) with respect to the intensity signal observed by *WMAP*. However, these small spinning dust grains are not expected to be significantly polarized (Draine 2003). Other mechanisms for producing polarized emission, including magnetic dust (Draine & Lazarian 1999), have not been observed to be dominant.

Given these polarized Galactic components, the standard method used to clean the *WMAP* polarization maps involves subtracting synchrotron and dust template maps from the total, leaving a cleaned CMB map at the Ka, Q, and V bands (Page et al. 2007; Gold et al. 2009). The spectral indices of the templates are not allowed to vary spatially, which is a sufficient approximation given the sensitivity of the observations. Errors are propagated by inflating the noise matrices to account for the uncertainties in the fitted coefficients of template maps (Page et al. 2007). In this alternative method, we parameterize the emission model, and use a sampling method to estimate the marginal mean posterior CMB Q and U maps in low-resolution pixels.

2.1. Bayesian Estimation of Sky Maps

The data, $\mathbf{d}$, consist of the Q and U polarization maps observed by *WMAP* at N_c frequency channels, and is a vector of length $2N_p \times N_c$. In this analysis, we will use HEALPix $N_{\rm side} = 8$ with $N_p = 768$.[15] The joint posterior distribution for a model $\mathbf{m}$ can be written as

$$p(\mathbf{m}|\mathbf{d}) \propto p(\mathbf{d}|\mathbf{m})p(\mathbf{m}), \tag{2}$$

with prior distribution $p(\mathbf{m})$ and Gaussian likelihood

$$-2\ln p(\mathbf{d}|\mathbf{m}) = \chi^2 + c, \tag{3}$$

with

$$\chi^2 = (\mathbf{d}-\mathbf{m})^T\mathbf{N}^{-1}(\mathbf{d}-\mathbf{m}) \tag{4}$$

and a normalization term c. Since the noise $\mathbf{N}$ is uncorrelated between channels, the likelihood can be written as the sum over frequency ν,

$$\chi^2 = \sum_{\nu}[\mathbf{d}_\nu - \mathbf{m}_\nu]^T\mathbf{N}_\nu^{-1}[\mathbf{d}_\nu - \mathbf{m}_\nu], \tag{5}$$

where $\mathbf{N}_\nu$ is the noise covariance at each channel. In this analysis, we use *WMAP* low-resolution maps with inverse noise matrices that describe the noise outside a processing mask covering $\sim$6% of the sky (see, e.g., Jarosik et al. 2007). These masked pixels should be neglected in the likelihood evaluation, but to simplify numerical implementation we include them, but set their inverse variance to be small (less than 0.1% of the unmasked pixels' inverse variance).

We parameterize the model in antenna temperature as the sum of three components:

$$\mathbf{m}_\nu = \sum_k \boldsymbol{\alpha}_{k,\nu}\mathbf{A}_k, \tag{6}$$

with CMB ($k = 1$), synchrotron emission ($k = 2$), and thermal dust emission ($k = 3$). In this analysis, we will ignore possible polarized contributions from other components including spinning dust, and free–free emission. Free–free emission may become slightly polarized due to Thomson scattering by electrons in H II regions.

The components each have amplitude vectors $\mathbf{A}_k$ of length $2N_p$ and diagonal coefficient matrices $\boldsymbol{\alpha}_{k,\nu}$ of side $2N_p$ at each frequency. The CMB radiation is blackbody, and we further assume that the Galactic components can be described with a spectral index that does not vary with frequency in the *WMAP* range. The coefficients are therefore given by

$$\boldsymbol{\alpha}_{1,\nu} = f(\nu)\mathbf{I}, \tag{7}$$

[15] The number of pixels is $N_p = 12N_{\rm side}^2$, with $N_{\rm side} = 2^{\rm res}$ where res is the "resolution" (Gorski et al. 2005).

$$\boldsymbol{\alpha}_{2,\nu} = \mathrm{diag}[(\nu/\nu_K)^{\boldsymbol{\beta}_2}], \quad (8)$$

$$\boldsymbol{\alpha}_{3,\nu} = \mathrm{diag}[(\nu/\nu_W)^{\boldsymbol{\beta}_3}]. \quad (9)$$

Here, we have introduced two spectral index vectors $\boldsymbol{\beta}_k$ each of length $2N_p$, pivoted at 23 GHz (ν_K) and 94 GHz (ν_W), respectively. The function $f(\nu)$ converts thermodynamic to antenna temperature. We then make three further simplifying assumptions. First, that the spectral indices in Q and U are the same in a given pixel, which equates to assuming that the polarization angle does not change with frequency. Second, the spectrum of thermal dust is assumed to be fixed over the sky, with fiducial value $\boldsymbol{\beta}_d = 1.7$, motivated by Finkbeiner et al. (1999). Third, we define $N_i < N_p$ pixels within which β_2 takes a common value, rather than allow it to take a unique value at each $N_{\rm side} = 8$ pixel. This is motivated by our understanding of the emission process: even though we expect spatial variation due to the different ages of the electron populations, the electron diffusion rate limits how much the index can vary over a short range (Strong et al. 2000, 2007). In this case, we use $N_{\rm side} = 2$ HEALPix pixels ($N_i = 48$).

Our model $\mathbf{m}$ is now described by $6N_p$ amplitude parameters $\mathbf{A} = (\mathbf{A}_1, \mathbf{A}_2, \mathbf{A}_3)^T$ and N_i spectral index parameters $\boldsymbol{\beta}$. Our main objective is to estimate the marginalized distribution for the CMB amplitude vector,

$$p(\mathbf{A}_1|\mathbf{d}) = \int p(\mathbf{A}, \boldsymbol{\beta}|\mathbf{d}) d\mathbf{A}_2 d\mathbf{A}_3 d\boldsymbol{\beta}, \quad (10)$$

from which we can estimate a map and covariance matrix.

2.2. Sampling the Distribution

We cannot sample the joint distribution $p(\mathbf{A}, \boldsymbol{\beta}|\mathbf{d})$ directly, so we use Markov Chain Monte Carlo methods to draw samples from it. It can be sliced into two conditional distributions $p(\mathbf{A}|\boldsymbol{\beta}, \mathbf{d})$ and $p(\boldsymbol{\beta}|\mathbf{A}, \mathbf{d})$, so we use Gibbs sampling to draw alternately from each conditional distribution, constructing a Markov chain with the desired joint distribution as its stationary distribution.

We briefly review Gibbs sampling for the case of one A parameter and one β parameter: starting from an arbitrary point (A_i, β_i) in the parameter space, we draw

$$(A_{i+1}, \beta_{i+1}), (A_{i+2}, \beta_{i+2}) \ldots \quad (11)$$

by first drawing A_{i+1} from $p(A|\beta_i, d)$ and then drawing β_{i+1} from $p(\beta|A_{i+1}, d)$. Then we iterate many times. The result is a Markov chain whose stationary distribution is $p(A, \beta|d)$. A description of Gibbs sampling can be found in Gelfand & Smith (1990), Wandelt et al. (2004), and Eriksen et al. (2007).

For the multivariate case $\mathbf{A}$ and $\boldsymbol{\beta}$ are now vectors, and so each vector is drawn in turn until convergence, producing a chain whose stationary distribution is the joint posterior distribution. Two distinct methods are used to draw the samples from each conditional distribution, depending on whether the amplitude vector $\mathbf{A}$, or the index vector $\boldsymbol{\beta}$, is held fixed.

2.2.1. Sampling the Amplitude Vector

For fixed $\boldsymbol{\beta}$, the conditional distribution $p(\mathbf{A}|\boldsymbol{\beta}, \mathbf{d})$ is a $6N_p$-dimensional Gaussian, so one can draw a sample of all $6N_p$ amplitude parameters simultaneously. The conditional distribution is

$$p(\mathbf{A}|\boldsymbol{\beta}, \mathbf{d}) \propto p(\mathbf{d}|\boldsymbol{\beta}, \mathbf{A}) p(\mathbf{A}). \quad (12)$$

For a uniform prior on $\mathbf{A}$, the mean, $\hat{\mathbf{A}}$, is found by minimizing

$$\chi^2 = \sum_\nu \left[\mathbf{d}_\nu - \sum_k \boldsymbol{\alpha}_{k,\nu}\mathbf{A}_k\right]^T \mathbf{N}_\nu^{-1} \left[\mathbf{d}_\nu - \sum_k \boldsymbol{\alpha}_{k,\nu}\mathbf{A}_k\right] \quad (13)$$

with respect to $\mathbf{A}$. This gives $\hat{\mathbf{A}} = \mathbf{F}^{-1}\mathbf{x}$, which can be written in block-matrix form,

$$\begin{pmatrix} \hat{\mathbf{A}}_1 \\ \hat{\mathbf{A}}_2 \\ \hat{\mathbf{A}}_3 \end{pmatrix} = \begin{pmatrix} \mathbf{F}_{11} & \mathbf{F}_{12} & \mathbf{F}_{13} \\ \mathbf{F}_{21} & \mathbf{F}_{22} & \mathbf{F}_{23} \\ \mathbf{F}_{31} & \mathbf{F}_{32} & \mathbf{F}_{33} \end{pmatrix}^{-1} \begin{pmatrix} \mathbf{x}_1 \\ \mathbf{x}_2 \\ \mathbf{x}_3 \end{pmatrix} \quad (14)$$

with elements

$$\mathbf{F}_{kk'} = \sum_\nu \boldsymbol{\alpha}_{k,\nu}^T \mathbf{N}_\nu^{-1} \boldsymbol{\alpha}_{k',\nu}, \quad (15)$$

$$\mathbf{x}_k = \sum_\nu \boldsymbol{\alpha}_{k,\nu}^T \mathbf{N}_\nu^{-1} \mathbf{d}_\nu. \quad (16)$$

Note that $\mathbf{F}$ is a $2N_p \times 2N_p$ matrix and $\mathbf{x}$ is a vector of length $2N_p$. The covariance of the conditional distribution is given by $\mathbf{F}^{-1}$. In the case of diagonal noise, the mean and variance are estimated pixel by pixel using the same method. Given the mean and Fisher matrix of the conditional distribution, we draw a Gaussian sample using the lower Cholesky decomposition of the Fisher matrix, $\mathbf{F} = \mathbf{L}\mathbf{L}^T$, with sample $\mathbf{A}_{i+1} = \hat{\mathbf{A}} + \mathbf{L}^{-1}\mathbf{G}$. The vector $\mathbf{G}$ contains $2N_p$ zero mean unit variance Gaussian random samples.

For a diagonal Gaussian prior on $A_{x,k}$ of $a_k \pm \sigma_k$, the expressions are modified to

$$\tilde{\mathbf{F}}_{kk'} = \mathbf{F}_{kk'} + \delta_{kk'}\sigma_k^{-2}\mathbf{I}, \quad (17)$$

$$\tilde{\mathbf{x}}_k = \mathbf{x}_k + \sigma_k^{-2}\mathbf{I}\mathbf{a}_k, \quad (18)$$

with posterior mean $\hat{\mathbf{A}} = \tilde{\mathbf{F}}^{-1}\tilde{\mathbf{x}}$ and variance $\tilde{\mathbf{F}}^{-1}$. In this analysis, we place uniform priors on the CMB and synchrotron Q and U amplitudes at each pixel, but impose a Gaussian prior on the dust Stokes vector $\mathbf{A}_2 = (\mathbf{Q}_2, \mathbf{U}_2)^T$ of $[\mathbf{Q}_2, \mathbf{U}_2] = 0 \pm 0.2\mathbf{I}_d$, using the dust map $\mathbf{I}_d$ at 94 GHz from model 8 of Finkbeiner et al. (1999), hereafter FDS, as a tracer of the intensity. The width of the prior, corresponding to a polarization fraction 20%, is motivated by Draine & Fraisse (2009), who predict the maximum polarization of dust grains to be about 15%.

Drawing this new amplitude vector is computationally demanding, and drives us to work with low-resolution maps. Our goal is to determine the polarized CMB signal at large angular scale, so this does not limit the analysis.

2.2.2. Sampling the Index Vector

For fixed A, we sample from the conditional distribution

$$p(\boldsymbol{\beta}|\mathbf{A}, \mathbf{d}) \propto p(\mathbf{d}|\boldsymbol{\beta}, \mathbf{A}) p(\boldsymbol{\beta}), \quad (19)$$

with prior probability $p(\boldsymbol{\beta})$. An analytic sample cannot be drawn from this distribution because the spectral indices are nonlinear parameters. However, for a small number of parameters it is feasible to draw samples using the Metropolis–Hastings algorithm. This algorithm has been described extensively in the cosmological parameter estimation literature (e.g., Knox et al. 2001; Lewis & Bridle 2002; Dunkley et al. 2005). The sampling goes as follows. For each index parameter in turn, a trial step β_T is drawn using a Gaussian proposal distribution

of width σ_T centered on the current $\boldsymbol{\beta}$ vector. Next, the current and trial $\boldsymbol{\beta}$ vectors are used to construct model vectors at each frequency, $\mathbf{m}_\nu = \sum_k \boldsymbol{\alpha}_{k,\nu}\mathbf{A}_k$. The current and trial posterior are then computed using

$$-2\ln p(\boldsymbol{\beta}|\mathbf{A},\mathbf{d}) = \chi^2 - 2\ln p(\boldsymbol{\beta}), \tag{20}$$

with χ^2 given in Equation (5). The ratio of the trial to current posterior, r, is used to determine whether to move to the trial position (with probability r), or to stay at the original position (with probability $1-r$). This use of the Metropolis algorithm to draw a subset of parameters is commonly known as Metropolis-within-Gibbs (e.g., Geweke & Tanizaki 2001), and has been used in astronomy to estimate Cepheid distances (Barnes et al. 2003). Other approaches to sampling spectral index parameters have been considered in e.g., Eriksen et al. (2007).

In regions of low signal-to-noise, it is necessary to impose a prior on the synchrotron spectral index, otherwise it is unconstrained and could take the "flat" index of the CMB component, opening up large degeneracies. We choose a Gaussian prior of -3.0 ± 0.3, motivated by understanding of the synchrotron emission (Rybicki & Lightman 1979) and allowing for variations of the size observed in the synchrotron intensity (e.g., Bennett et al. 2003). This is combined with a uniform prior on the CMB and synchrotron amplitudes, and a Gaussian prior $0\pm0.2I_d$ on the dust Q and U amplitudes. This parameterization and choice of prior does not guarantee that the marginalized means for the A and β parameters will be unbiased estimators, as discussed in, e.g., Eriksen et al. (2007). In the limit of low signal-to-noise, there is a larger volume of models with a flatter (i.e., β tending to 0) synchrotron spectrum, allowing large CMB and synchrotron amplitudes of opposite sign. One approach is to modify the prior on the spectral indices to include an additional "phase-space" factor. We discuss this further in Section 3.

2.3. Processing the Sampled Distribution

We form maps of each component from the mean of the marginalized distribution,

$$\langle\mathbf{A}_k\rangle = \int p(\mathbf{A}_k|\mathbf{d})\mathbf{A}_k d\mathbf{A}_k = \frac{1}{n_{\rm G}}\sum_{i=1}^{n_{\rm G}}\mathbf{A}_k^i, \tag{21}$$

where the sum is over all $n_{\rm G}$ elements in the chain, and $\mathbf{A}_k^i$ is the ith chain element of the kth component map. The covariance matrices for $\mathbf{A}_k$, including off-diagonal terms, are estimated using the same method, summing over the chain components. As an example, the covariance $C_{xy,k}$ between pixels x and y for component k is computed using

$$C_{xy,k} = \langle A_{x,k}A_{y,k}\rangle - \langle A_{x,k}\rangle\langle A_{y,k}\rangle \tag{22}$$

$$= \frac{1}{n_{\rm G}}\sum_{i=1}^{n_{\rm G}}\left(A_{x,k}^i - \langle A_{x,k}\rangle\right)\left(A_{y,k}^j - \langle A_{y,k}\rangle\right). \tag{23}$$

For the synchrotron and dust components, we compute only the diagonal elements of the covariance matrices.

2.3.1. Power in the E-Mode

To quantify the polarization anisotropy present in the Q and U maps, we use the coordinate-independent scalar and pseudo-scalar E and B modes commonly used in cosmological analysis (Seljak 1997; Kamionkowski et al. 1997). Both polarization modes probe the evolution of the decoupling and reionization epochs and are generated by Thomson scattering of a quadrupolar radiation pattern by free electrons. The anisotropy is quantified using the $C_\ell^{\rm TE}$, $C_\ell^{\rm EE}$, $C_\ell^{\rm BB}$ power spectra, where

$$C_\ell^{XY} = \left\langle a_{lm}^X a_{lm}^{Y*}\right\rangle. \tag{24}$$

The spin-2 decomposition of the polarization maps, $a_{lm}^{E,B}$, is related to the Q and U maps by

$$[Q\pm iU](\hat{x}) = \sum_{\ell>1}\sum_{m=-\ell}^{\ell} {}_{\mp2}a_{\ell m}\,{}_{\mp2}Y_{\ell m}(\hat{x}), \tag{25}$$

where ${}_{\pm2}a_{lm} = a_{lm}^E \pm i a_{lm}^B$ (Zaldarriaga & Seljak 1997).

The first stars reionize the universe at redshift z_r, producing a signal in the E-mode power spectrum proportional to τ^2, where τ is the optical depth to reionization. In this analysis, we use the approximation to the optical depth used in Page et al. (2007), estimated by varying only τ and the power spectrum amplitude, such that the temperature anisotropy power at $\ell = 220$ is held constant. Other cosmological parameters are fixed to fiducial values and the exact likelihood is computed as a function of τ. The likelihood, $p(C_\ell|\mathbf{d})$, given in Appendix D of Page et al. (2007), is evaluated using the marginal posterior mean Q/U maps and their covariance matrix, which are processed as described in Page et al. (2007) to account for the P06 Galactic mask.

2.4. Testing Convergence

The convergence of the chain is determined by applying the spectral convergence test described in Dunkley et al. (2005) to the spectral index parameters and a random subset of the amplitude parameters. This tests for convergence of the mean, but convergence of the covariance matrix is also required for estimating the power in the maps at large scales. We check this by applying a jackknife test to the derived optical depth parameter τ. For a chain that samples only the amplitude vectors, and has diagonal noise, 1000 iterations are typically sufficient. With the Metropolis sampling step included, about 10,000 iterations are required, and when off-diagonal noise is included, typically 50,000 iterations are necessary.

3. SIMULATED POLARIZATION MAPS

We simulate all-sky signal and noise maps at HEALPix $N_{\rm side} = 16$, with $N_p = 3072$ pixels, for the Stokes Q and U parameters, at the five *WMAP* frequencies (22.8, 33, 40.7, 60.8, and 93.5 GHz). In the notation of Section 2, the data are modeled as

$$\mathbf{s}_\nu = f(\nu)\mathbf{A}_1 + (\nu/\nu_K)^{\beta_s}\mathbf{A}_2 + (\nu/\nu_W)^{\beta_d}\mathbf{A}_3, \tag{26}$$

where $\mathbf{s}_\nu$ is a vector of length $2N_p$ containing the total Q and U signals in antenna temperature at frequency ν. The CMB signal map, $\mathbf{A}_1$, is generated for a fiducial cosmological model by drawing multipoles a_{lm} from the theoretical power spectrum C_ℓ, and transforming to map space, using the "synfast" routine in HEALPix. We choose a model with $\tau = 0.1$, with other cosmological parameters given by the best-fit three-year *WMAP* ΛCDM model (Spergel et al. 2007). For the synchrotron emission, with amplitude map $\mathbf{A}_2$ defined at 23 GHz, we use the three-year *WMAP* Q and U low-resolution K-band maps (Page et al. 2007). The frequency dependence is assumed to be a power law with $\beta = -3.0$ over the full sky. For the thermal dust map, $\mathbf{A}_3$, defined at the W band (94 GHz), we construct

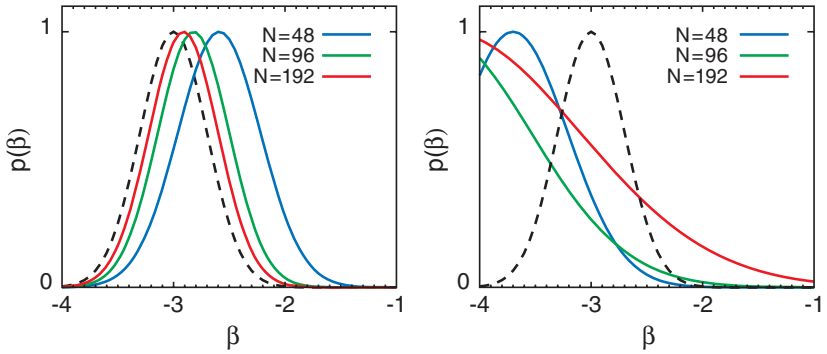

Figure 1. Left: for maps with $N_p = 768$ pixels and N_i (marked N in figure) synchrotron spectral indices with Gaussian priors of $\beta = -3.0 \pm 0.3$ (dashed curve), the recovered index estimates are larger than the prior (solid curves) for simulations with no signal. The estimated index mean increases with the number of pixels sharing the same index. Right: the spectral index priors that are imposed (colored curves), in addition to $\beta = -3.0 \pm 0.3$, to account for the volume effect.

maps that are 5% polarized, using the dust intensity template $\mathbf{I}_d$ from *IRAS*, extrapolated to 94 GHz using model 8 of Finkbeiner et al. (1999) and degraded to $N_{\rm side} = 16$. We form

$$\mathbf{Q}_3 = 0.05\mathbf{I}_d \cos(2\gamma) \quad (27)$$

$$\mathbf{U}_3 = 0.05\mathbf{I}_d \sin(2\gamma), \quad (28)$$

where the polarization angles γ are computed from the starlight polarization template described in Page et al. (2007), using observations from Heiles (2000) and Berdyugin et al. (2001, 2004). We assume a power-law index with $\beta_d = 1.7$ over the whole sky. This is a simplified model of the true sky, as we would expect the emission processes to result in some spatial and frequency dependence of the spectral indices. A realistic Galactic field model would also lead to a spatially dependent suppression of the dust polarization fraction (Page et al. 2007; Miville-Deschenes et al. 2008).

The simulated maps are formed at each frequency ν using $\mathbf{d}_\nu = \mathbf{s}_\nu + \mathbf{n}_\nu$, where $\mathbf{n}_\nu$ is a realization of the *WMAP* noise. We consider both diagonal noise realizations, and full noise realizations including pixel–pixel and Q–U correlations, drawn from the *WMAP* $N_{\rm side} = 16$ noise matrices. These correspond to maps co-added by year and DA, as described in Jarosik et al. (2007) and Hinshaw et al. (2009). The low-resolution inverse noise matrices are not defined inside the processing mask, so we set the noise in these pixels to be large. Realizations are computed at each channel using SVD decompositions of the *WMAP* inverse noise matrices $\mathbf{N}_\nu^{-1}$, in antenna temperature. We then create $N_{\rm side} = 8$ simulations, with 768 pixels, by degrading the $N_{\rm side} = 16$ simulated maps and $\mathbf{N}^{-1}$ inverse noise matrices using inverse weighting.

We perform the Gibbs sampling using the four *WMAP* frequency bands K, Ka, Q, V (hereafter KKaQV). We do not include W band as standard, due to concerns about potential systematic effects (Hinshaw et al. 2009). For the diagonal noise case this requires of the order of 10,000 iterations for convergence. The chains are processed as described in Section 2.3 to obtain marginal posterior mean maps and errors for $\mathbf{A}_1$ (containing Q and U for CMB), $\mathbf{A}_2$ (synchrotron), $\mathbf{A}_3$ (thermal dust), and $\boldsymbol{\beta}$ (synchrotron spectral index).

3.1. Spectral Index Prior

For the simulated maps with $\beta = -3.0$ and a Gaussian prior on the indices of -3.0 ± 0.3, we find the recovered marginal posteriors $p(\beta|d)$ to be biased estimators. To explore this further, we sample the joint distribution for a noise-only simulation, drawn from the *WMAP* five-year noise maps. The resulting marginalized distributions for the $N_i = 48$ spectral indices are close to Gaussian, but centered on $\beta = -2.6$. The Gaussian distribution best fitting the samples is shown in the left panel of Figure 1. When the number of spectral index pixels is increased to 96, and 192, the recovered distribution tends toward the input value of $\beta = -3.0$. This effect arises for our Galactic emission model, as there is a larger volume of phase space for shallow indices far from the prior central value. This is not a significant effect for individual pixels, but the phase-space volume relative to that of the prior central value increases for more pixels sharing a common index parameter.

In the case of a single pixel, a common approach is to adopt the Jeffreys' prior (Jeffreys 1961), a noninformative prior distribution that is proportional to the square root of the Fisher information, as described for example in Eriksen et al. (2007). Imposing the Jeffreys' prior on the spectral index parameters in this model would give less weight to steep indices than shallow ones, accounting for their smaller effect on the likelihood. However, this would not overcome the phase-space effect that arises from the increase in volume of models with shallow indices.

While there may be alternative parameterizations that avoid this problem, we choose instead to modify the spectral index prior. We use $p(\beta) = p_s(\beta)/L_0(\beta)$, where p_s is the Gaussian prior -3.0 ± 0.3, and $1/L_0$ is an additional "phase-space" factor. We estimate this factor by evaluating the marginalized posterior, $p(\beta|d)$, for a noise-only simulation with prior $p_s(\beta)$, and defining $L_0(\beta) = p(\beta|d)/p_s(\beta)$. The assumption is that L_0 is an approximate description of the available phase-space volume. The factors, $1/L_0$, are modeled as Gaussian distributions and are shown in the right panel of Figure 1 for $N_i = 48$, 92, and 192, with $\beta = -3.7 \pm 0.5$ for the $N_i = 48$ adopted in this analysis. These distributions are not exact, particularly at $\beta < -4$, but we check that the approximation is sufficient by resampling the distributions with the new prior, finding the recovered mean to be $\beta = -3.0$. We repeat the test for a Gaussian prior of -2.7 ± 0.3, and further test that this prior only weakly depends on the inclusion of W band.

This is not the optimal solution, as the prior is informative in the presence of a signal and could therefore lead to parameter bias, in particular in the weak signal regime. We test simulations for two different signal maps with synchrotron indices -3.0 and -2.7, using Gaussian priors p_s of -3.0 ± 0.3 and -2.7 ± 0.3 combined with the phase-space factor. As expected, when the prior p_s matches the signal, the estimated index values are all consistent with the input signal. When it does not match the

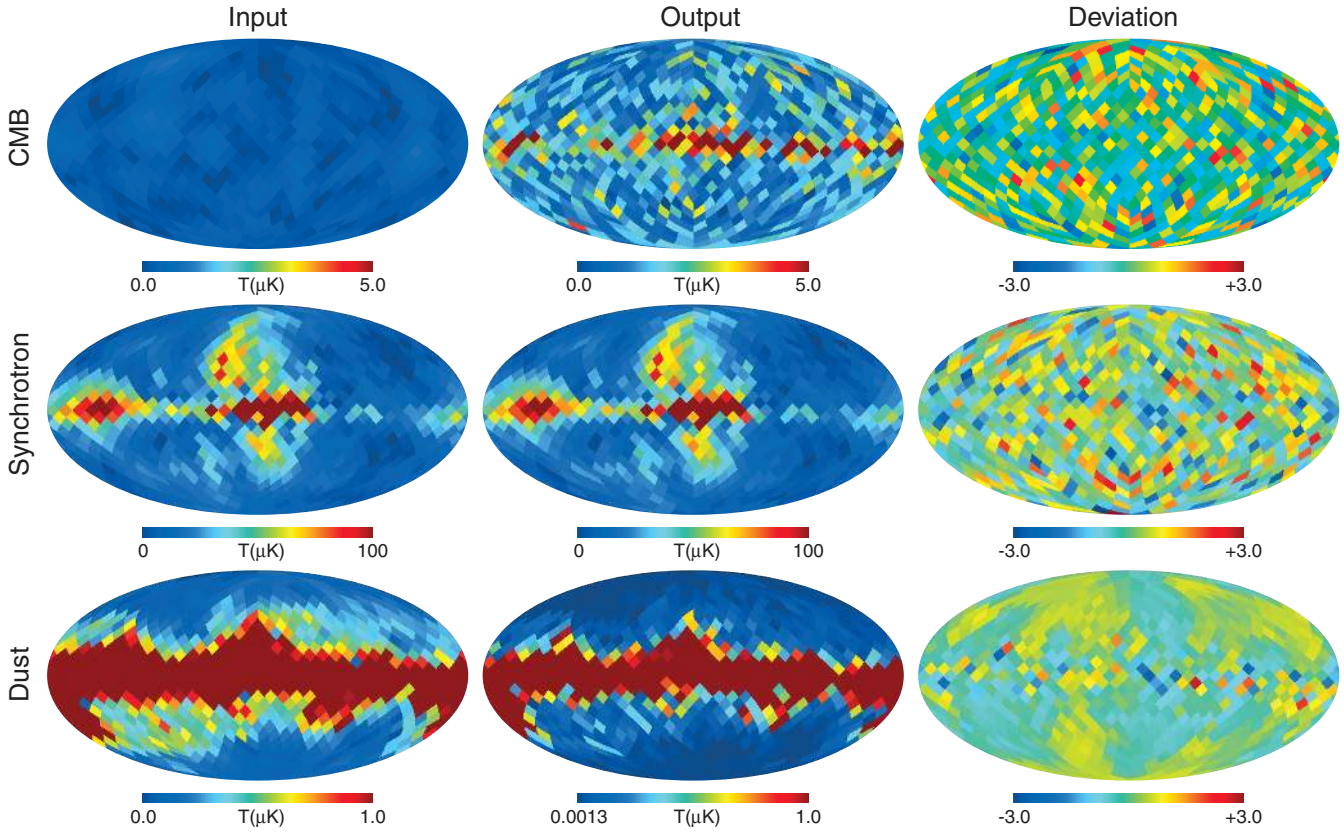

Figure 2. Comparison of input (left) and output (middle) component maps for a simulation with $N_{\rm side} = 8$. The polarization amplitude $P = \sqrt{Q^2 + U^2}$ is shown for the CMB (top), synchrotron at 23 GHz (middle), and dust at 94 GHz (bottom). The right panel shows the difference in standard deviations per pixel for the Q Stokes parameter. The dust component has a Gaussian prior on the dust Stokes parameters of $[Q, U](n) = 0 \pm 0.2 I_d(n)$, where $I_d(n)$ is the FDS dust intensity (see the text), which reduces the deviation per pixel and leads to the structure in the difference map.

signal, an unbiased marginal index value is estimated in the highest signal-to-noise pixels, and the low signal-to-noise pixels tend to the central value of p_s. This is the behavior we expect, but does not confirm that our final estimated parameters will be unbiased. However, since we have good astrophysical motivation to require that the synchrotron index is close to $\beta = -3$, we do not expect this to be a significant effect. We address this issue in this analysis by checking that our main conclusions are insensitive to the detailed choice of the spectral index prior, and defer an investigation of a more optimal parameterization to a future analysis.

3.2. Simulations with Diagonal Noise

We now apply the method to simulations with signal and diagonal noise properties. Figure 2 shows the input and output polarization amplitude maps for the CMB, synchrotron, and dust components, derived from the Q and U maps, $P = \sqrt{Q^2 + U^2}$, for the fiducial simulation with synchrotron index $\beta = -3.0$. The third column shows the difference in standard deviations per pixel for the Q Stokes parameter, $\delta = (Q_{\rm in} - Q_{\rm out})/\sigma_Q$. For the CMB maps the absolute difference between input and output maps is greatest in the Galactic plane where the foreground signal is high. However, since these effects are captured in the errors in the map, the deviation maps do not have a strong spatial dependence. The χ^2 for the map, $(\mathbf{A}_1^{\rm in} - \mathbf{A}_1^{\rm out})^T \mathbf{C}_1^{-1} (\mathbf{A}_1^{\rm in} - \mathbf{A}_1^{\rm out})$, is 1270 for 1536 pixels. This gives $\chi^2/\text{pixel} < 1$, due to the prior on the dust amplitude. When the prior on the dust amplitude is removed, the goodness of fit of the recovered CMB maps is $\chi^2 = 1497$ ($\chi^2/\text{pixel} = 0.98$), but the errors are significantly inflated. The synchrotron maps are recovered with $\chi^2/\text{pixel} = 1.04$ for the Q and U maps. The dust maps are recovered with $\chi^2/\text{pixel} = 0.24$, with structure apparent in the deviation map. This is due to the prior: far from the plane the signal-to-noise is low and the dust tends to the prior central value of zero. Removing the prior on the dust amplitude, the goodness of fit of the recovered dust maps is $\chi^2/\text{pixel} = 0.97$, close to 1 as expected. The total χ^2 of the estimated model, $\sum_\nu [\mathbf{d}_\nu - \mathbf{m}_\nu]^T \mathbf{N}_\nu^{-1} [\mathbf{d}_\nu - \mathbf{m}_\nu]$, is $2.08 N_p$ without the dust prior, and $3.51 N_p$ with the dust prior. This is consistent with the number of degrees of freedom ($2N_p - N_i$ in the absence of priors).

The optical depth computed from this simulation is $\tau = 0.091 \pm 0.019$ outside the P06 Galactic mask, with distribution shown in Figure 3. We test for bias by generating 10 further diagonal noise and signal realizations of the model with $\tau = 0.1$, and find ensemble average of $\tau = 0.098$, consistent with the input but limited by small number statistics. We also test a simulation for KKaQV with no polarized CMB component. The recovered optical depth to be consistent with zero, shown in Figure 3. Adding the W band (KKaQVW) we find $\tau = 0.098 \pm 0.017$.

In this ideal case, the simulation matches the parameterized model, but in a realistic scenario the model will not perfectly describe the sky. For a Gaussian prior on the spectral index of $\beta_s - 2.7 \pm 0.3$, we find a negligible effect on τ, with $\tau = 0.094 \pm 0.020$. A larger increase of $\sim 1\sigma$ in τ, to 0.111 ± 0.019, is seen when the spectral index of the simulation shallows from -3.0 to -2.5 between the K and W bands, but

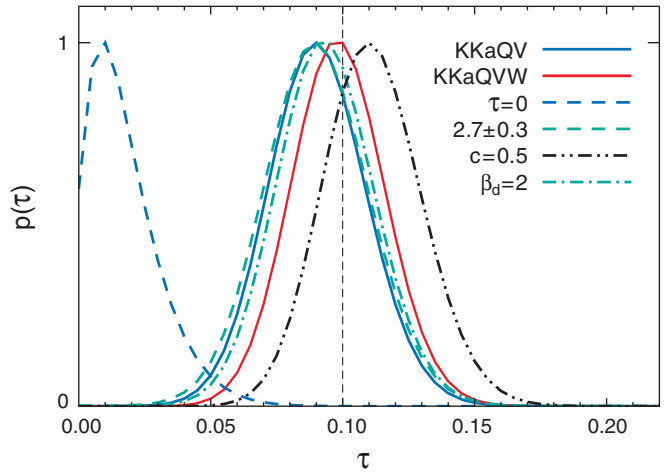

Figure 3. Distribution of the optical depth to reionization τ for simulations with five-year *WMAP* noise levels. The optical depth is recovered for an individual simulation with $\tau = 0.1$ (black dashed line), for KKaQV and KKaQVW, and a $\tau = 0$ simulation is consistent with zero power. Changing the index priors to $\beta_d = 2$, or $\beta_s = -2.7 \pm 0.3$ have negligible effects on the recovered CMB power. Incorrectly modeling the synchrotron as a power law for a simulation with an index that increases by $c = 0.5$ between 23 and 94 GHz increases τ by $\sim 1\sigma$.

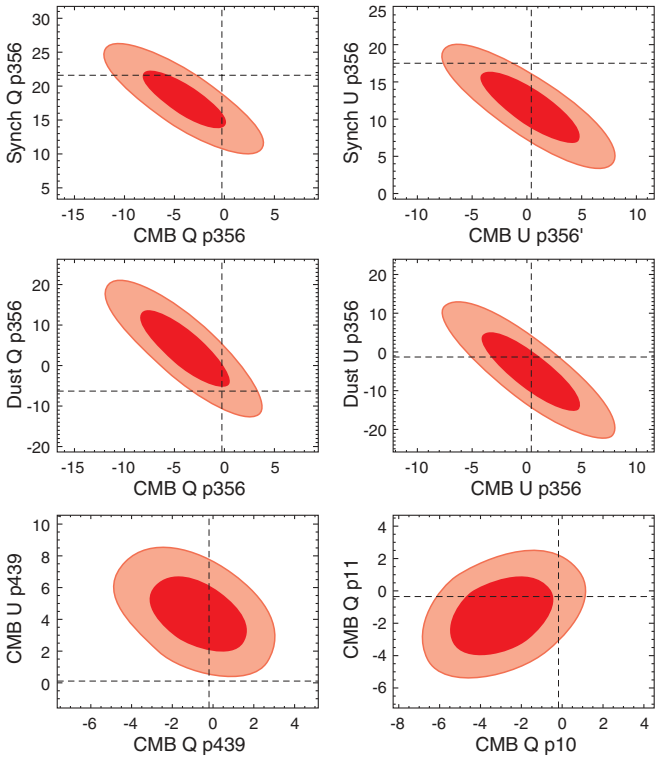

Figure 4. Marginalized 68% and 95% confidence levels for a subset of the A and β parameters for simulated maps (inputs shown dashed). The top and middle panels show the correlation between the CMB, synchrotron and dust Q and U amplitudes (in μK) for an arbitrary single pixel (pixel 356 out of 768 using HEALPix nested ordering). The bottom panels show the correlation between Q and U for a single pixel (p439), and between two adjacent pixels (p10 and p11). By marginalizing, rather than finding the maximum likelihood, the error on the CMB amplitude is inflated to account for foreground uncertainty.

is modeled by a pure power law. In this case, the model does not remove enough synchrotron at high frequencies, leaving excess power in the CMB. For the thermal dust component we fix $\boldsymbol{\beta}_d = 1.7$ for all pixels in the fiducial case. Changing this to $\boldsymbol{\beta}_d = 2$ has a negligible effect on our results. Removing the dust prior altogether opens up long degeneracies between the dust and the CMB amplitudes, highlighting the importance of the dust intensity map to limit the polarized dust contribution. Modest changes of the dust polarization fraction prior to 15% or 25% have little effect on the estimated CMB signal.

3.3. Simulation with Full Noise Matrix

When the full off-diagonal noise matrix is included we find of the order of 50,000 iterations are necessary for convergence. The χ^2 for the map computed using the full covariance matrix, $(\mathbf{A}_1^{\rm in} - \mathbf{A}_1^{\rm out})^T \mathbf{C}_1^{-1} (\mathbf{A}_1^{\rm in} - \mathbf{A}_1^{\rm out}) = 1220$ for 1536 pixels, consistent with the diagonal noise case ($\chi^2 = 1270$). The recovered spectral index distributions are consistent with the simulated values, and the estimated optical depth of a single simulation with input $\tau = 0.1$ is 0.110 ± 0.020. Testing a large set of simulations with full inverse noise matrices is beyond the scope of this analysis. To demonstrate the effect on the estimated CMB maps of marginalizing, Figure 4 shows two-dimensional marginalized distributions for a subset of parameters, for a single pixel and between pixels. The top and middle rows show the correlation between the CMB, synchrotron, and dust Q and U components within a single pixel. The one-dimensional error on the marginalized CMB Q and U amplitudes is larger than the error obtained if the foreground amplitudes are fixed at their maximum likelihood amplitudes. The bottom row shows correlations between Q and U components within a pixel, and between adjacent pixels. If the inter-pixel correlations are ignored, the maps are recovered with incorrect noise properties.

4. RESULTS FROM *WMAP* DATA

We apply the sampling method to the five-year *WMAP* data, using low-resolution co-added $N_{\rm side} = 16$ maps and inverse noise matrices as the inputs, and then degrading to $N_{\rm side} = 8$ as for the simulations. Figures 5 and 6 show maps of the mean values and 1σ errors for the marginalized CMB, synchrotron, and dust amplitudes.

4.1. CMB Polarization

We first consider the CMB results. The noise patterns for both Q and U in Figure 6 are consistent with what we expect: in regions of low Galactic emission, the errors are dominated by instrumental noise. As the Galactic plane is approached, errors from foreground uncertainty begin to dominate, in particular where the dust contribution is most uncertain. This is a real advantage of the method: rather than imposing masks, the method inflates the errors where the foregrounds are brightest. As opposed to template cleaning, which produces CMB maps at each frequency observed, this method recovers a single Q and U polarization map, and so has higher signal-to-noise than any of the individual template-cleaned maps. There is some indication of structure in the CMB signal, particularly in the Q Stokes map at the Galactic anti-center, and in the U map in the region of the North Polar Spur. This is consistent with noise. Outside the P06 mask the maps are morphologically similar to the template-cleaned CMB maps co-added over Ka, Q, and V bands. The correlation coefficients for the pixels within the CMB maps have a maximum value of $\sim$40%, with rms correlation of $\sim$2%.

We compare the power at each multipole, outside the P06 mask, to the template-cleaned case from the main *WMAP* analysis (Gold et al. 2009) in Figure 7. Using the method

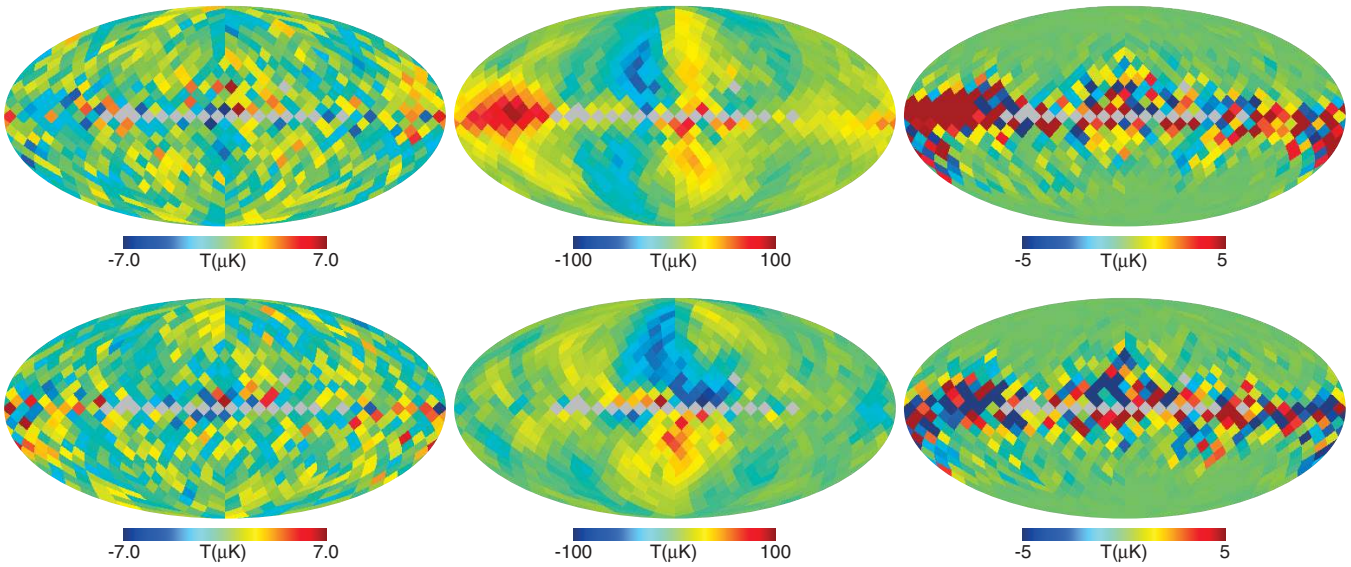

Figure 5. Low-resolution polarized Q (top) and U (bottom) maps of the CMB, synchrotron, and dust emission, estimated from the five-year K, Ka, Q, and V band maps using the Gibbs sampling method. Pixels inside the processing mask are gray. The CMB maps (left panels, thermodynamic temperature) do not show significant Galactic contamination in the plane. The synchrotron amplitudes (center, antenna temperature), are defined at K band (22.8 GHz), and are consistent with the total K-band maps, with high Q and U emission from the North Polar Spur, and high Q emission in the Galactic plane at longitude $110 \lesssim l \lesssim 170$. The dust amplitudes (right, antenna temperature) are defined at W band (93.5 GHz), and have a Gaussian prior on Q and U of $0 \pm 0.2 I_d$ where I_d is the dust intensity.

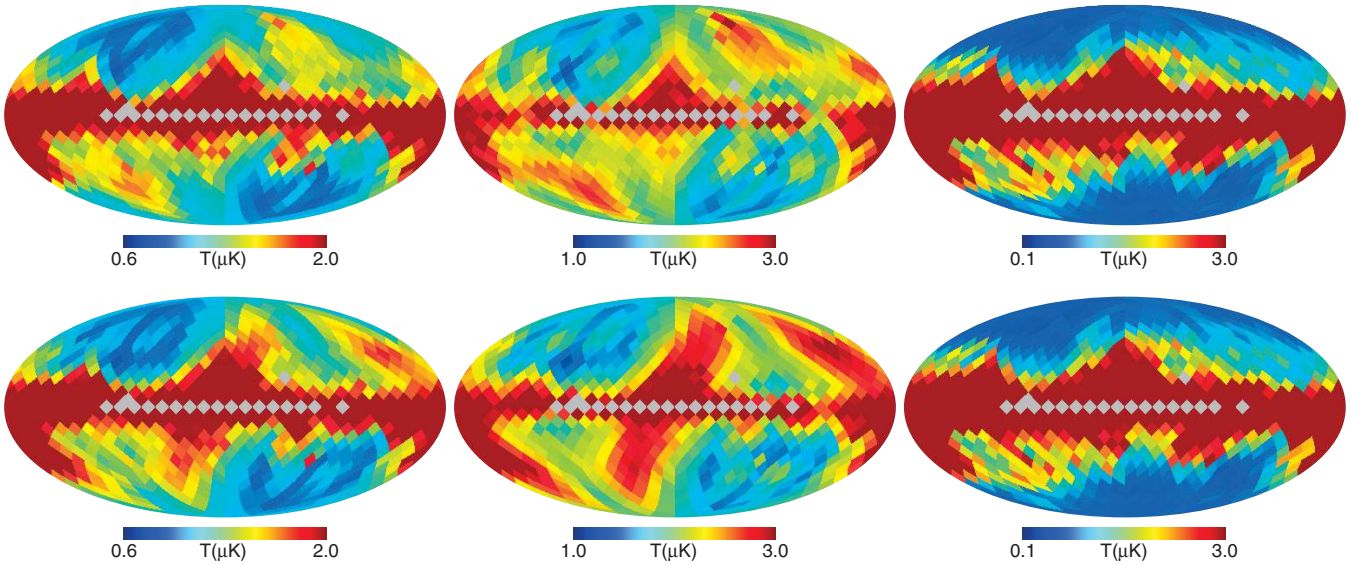

Figure 6. Estimated 1σ errors on the low-resolution maps of the CMB (left), synchrotron (center), and dust (right) Q and U components, as shown in Figure 5. The CMB errors are more fully described by a covariance matrix, including pixel–pixel correlation and Q/U correlation, so the maps can be used for cosmological analysis. The errors on the dust maps (right) are dominated by the prior that limits the dust polarization fraction to 20%. The middle panels clearly show the two sources of uncertainty in our CMB polarization maps: detector noise in the ecliptic plane (which traces a sideways S in the map) and foreground removal uncertainties in the Galactic plane.

described in Nolta et al. (2009), at each multipole the conditional likelihoods are computed as a function of C_ℓ^{EE}, with all other multipoles held fixed, for $2 < \ell < 7$. The results are consistent, although this analysis finds more power at $\ell = 4$ and 5. Computing the likelihood as a function of τ we find $\tau = 0.090 \pm 0.019$ for the Gibbs-sampled maps outside the P06 mask, which is consistent with the results obtained through template cleaning, which give $\tau = 0.086 \pm 0.016$ for the KaQV data combination. Obtained using a different methodology and accounting for foreground marginalization, this adds confidence in the detection of the CMB E-mode polarization signal. The spatially varying synchrotron index appears not to cause a significant difference, as we obtain a similar mean when the synchrotron spectral coefficients are fixed at the best-fit values found in the template cleaning. This also confirms that the choice of the spectral index prior is not affecting the estimated CMB power in the maps. We find similar limits on the optical depth when W band is included (KKaQVW), with $\tau = 0.085 \pm 0.017$. However, we choose not to use W band in the standard analysis, as discussed earlier. The Gaussian prior on the dust Q and U parameters does affect the CMB signal constraint: removing it significantly weakens the limit on the large-scale power, but changing it to, e.g., 15% or 25% has little effect, consistent with tests on simulations. A significantly tighter prior is not physically motivated, and could lead to bias in the recovered signal.

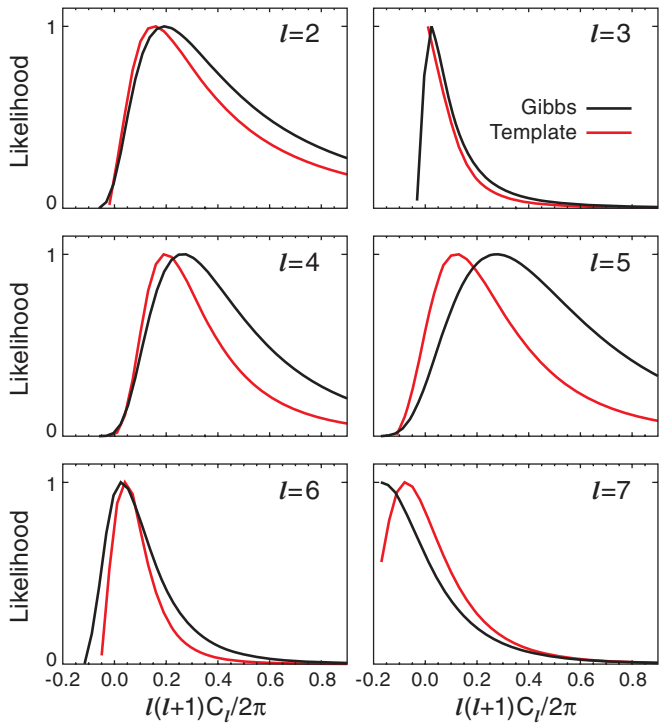

Figure 7. Conditional likelihoods for the CMB EE multipole moments estimated from the polarization maps described in this analysis (black), compared to the template cleaned maps described in Gold et al. (2009; red). They are computed as in Nolta et al. (2009) by fixing all other C_ℓ values at the fiducial ΛCDM values. There is agreement between the two methods.

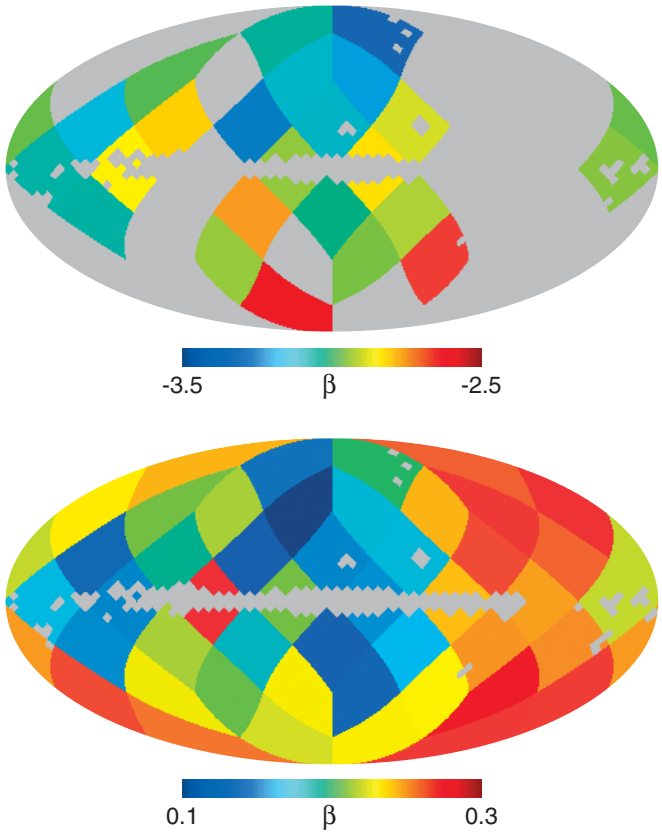

Figure 8. Estimated synchrotron spectral index (top), and 1σ errors (bottom), estimated in 48 HEALPix $N_{\rm side} = 2$ pixels. A Gaussian prior of $\beta_s = -3.0 \pm 0.3$ is imposed in each pixel. In regions of low signal-to-noise (near the ecliptic plane), the prior drives the spectral index estimate, so we mask the index for pixels with $\sigma(\beta) > 0.25$. The mean index averaged over the unmasked pixels is -3.03 ± 0.04 for prior -3.0 ± 0.3.

4.2. Synchrotron Polarization

The synchrotron maps shown in Figure 5 are similar to the total K-band maps (Hinshaw et al. 2009). The difference between the estimated synchrotron amplitude, and the K-band amplitude, is <5 μK outside the P06 mask, and <8 μK in the Galactic plane. As observed in the three-year *WMAP* data (Page et al. 2007), the signal is dominated by emission from the North Polar Spur, marked on the microwave sky map in Hinshaw et al. (2007), as well as what is often known as the "Fan region" (e.g., Wolleben et al. 2006), centered on Galactic coordinates $l \sim 140$, $b \sim 5$. The synchrotron emission dominates the signal at low frequencies, and so the uncertainty in the synchrotron Q and U maps, shown in Figure 6, is dominated by instrument noise, with only a small contribution from marginalization in the Galactic plane. Figure 8 shows the mean synchrotron spectral index estimated in the 48 pixels, together with 1σ errors. In regions of low synchrotron signal-to-noise the index is driven by the prior, so we mask pixels with $\sigma(\beta) > 0.25$. There is a preference in the North Polar Spur and Fan region for an index of ~ -3: the index averaged over regions with $\sigma(\beta) < 0.25$ is -3.03 ± 0.04. The estimated indices of these pixels are also shown in Figure 9, ordered by increasing errors to highlight the high signal-to-noise pixels on the left. Cutting the sky into high and low latitude at $b = 20$ deg, the low latitude weighted mean, -3.00 ± 0.04, is consistent with the high latitude -3.08 ± 0.06. This contrasts with the more significant steepening of the index with latitude observed in Kogut et al. (2007) in the analysis of the three-year *WMAP* polarization data, although here we exclude part of the plane. These results coming from alternative analyses will be more easily assessed with higher signal-to-noise data. We check that the latitude dependence is unaffected when the phase-space factor in the spectral index prior, a Gaussian -3.7 ± 0.5, is modified to have width 1.0 or mean -4.0.

An extrapolation of the Haslam 408 MHz synchrotron intensity maps to *WMAP* frequencies suggests that a shallower index is preferred in the plane, compared to the polarization, in the absence of anomalous dust. However, our estimated polarization index is consistent with the synchrotron intensity maps derived by the MEM method (Gold et al. 2009). Degrading the synchrotron component map in each band to $N_{\rm side} = 2$, and fitting a power law to the data in K, Ka, Q, and V bands for each pixel, the spectral index values are best-fit by a power-law with index $\beta = -3.1$ for the pixels at $b = 0$.

We check the estimate of the spectral indices by re-running the analysis with a Gaussian synchrotron index prior, $p_s(\beta)$, of -2.7 ± 0.3 in addition to the phase-space factor. The estimated indices are compared pixel by pixel in Figure 9. The prior has only a small effect on the high signal-to-noise index estimates. The $\sigma(\beta) < 0.25$ pixel average in this case is -2.94 ± 0.04. The estimated CMB power is little affected by this change in prior, with $\tau = 0.092 \pm 0.019$.

4.3. Dust Polarization

The dust polarization map has a low signal-to-noise ratio, particularly far from the plane, as we only fit data in the K–V bands. In these regions the prior dominates the estimate of the dust amplitude, making it hard to draw conclusions about the dust component. The error in Q and U is driven by the prior on the polarization amplitudes and so is morphologically identical

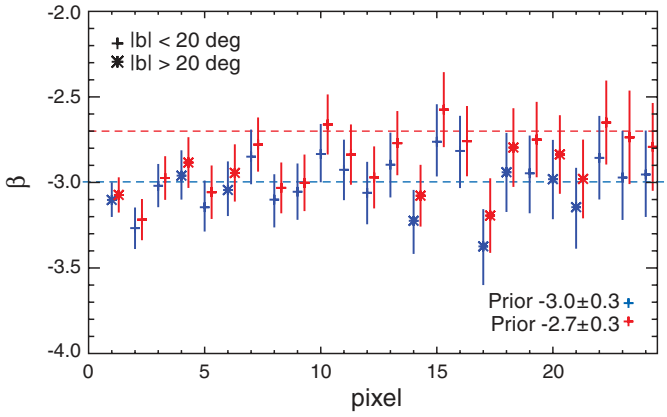

Figure 9. Marginalized mean and 1σ error bars for the synchrotron spectral index parameters with highest signal-to-noise for the five-year *WMAP* data, for Gaussian priors of -3.0 ± 0.3 and -2.7 ± 0.3. The pixels are ordered with increasing 1σ errors, with the highest signal-to-noise pixels on the left. The prior has only a small effect on the estimated indices.

to the FDS dust intensity map. This explains why the error far from the plane is low even though the dust is only poorly measured. The fractional polarization outside P06 is typically only 1%–2%, where we use the degraded FDS dust map to trace intensity, and rises to $\sim 10\%$ in some regions of the plane. This is lower than the $\sim$4% estimated in (Kogut et al. 2007; Gold et al. 2009). However, these maps are only estimated for $\nu \leqslant 61$ GHz, and in regions of low dust the prior prefers zero polarization. The fractional polarization estimate also assumes that the FDS map accurately traces the dust intensity in the *WMAP* frequency range. Inclusion of higher frequency data will allow us to learn more about the polarized dust.

5. CONCLUSION

We have used Bayesian parameter estimation to estimate low-resolution polarized CMB maps, marginalized over foreground contamination. These may then be used as inputs for a likelihood analysis. The emission model is parameterized accounting for physical understanding of the Galactic emission. The method has been tested on simulated maps, and found to produce unbiased estimates for the CMB power, quantified by the optical depth to reionization. With the five-year *WMAP* data we find a consistent result compared to template cleaning, with $\tau = 0.090 \pm 0.019$ from this method and 0.086 ± 0.016 from the standard template-cleaning method. This method captures the increase in errors where foreground uncertainty is larger, so depends less on a Galactic mask. Estimates of the polarized Galactic components indicate a synchrotron spectral index of order $\beta = -3.0$ in the Fan region in the Galactic anti-center, and the North Polar Spur area.

The *WMAP* mission is made possible by the support of the Science Mission Directorate Office at NASA Headquarters. This research was additionally supported by NASA grants NNG05GE76G, NNX07AL75G S01, LTSA03-000-0090, ATPNNG04GK55G, and ADP03-0000-092. We thank the referee for helpful comments. E.K. acknowledges support from an Alfred P. Sloan Research Fellowship. This research has made use of NASA's Astrophysics Data System Bibliographic Services. We acknowledge use of the HEALPix, CAMB, and CMBFAST packages.

REFERENCES

Barnes, T. G., III, Jefferys, W. H., Berger, J. O., Mueller, P. J., Orr, K., & Rodriguez, R. 2003, ApJ, 592, 539
Beck, R. 2001, Space Sci. Rev., 99, 243
Bennett, C. L., et al. 2003, ApJ, 583, 1
Berdyugin, A., Piirola, V., & Teerikorpi, P. 2004, A&A, 424, 873
Berdyugin, A., Teerikorpi, P., Haikala, L., Hanski, M., Knude, J., & Markkanen, T. 2001, A&A, 372, 276
Crutcher, R., Heiles, C., & Troland, T. 2003, in Lecture Notes in Physics, Vol. 614, Turbulence and Magnetic Fields in Astrophysics, ed. E. Falgarone & T. Passot (Berlin: Springer), 155
Davis, L. J., & Greenstein, J. L. 1951, ApJ, 114, 206
Dobler, G., & Finkbeiner, D. P. 2008, ApJ, 680, 1222
Draine, B. T. 2003, ARA&A, 41, 241
Draine, B. T., & Fraisse, A. A. 2009, ApJ, 696, 1
Draine, B. T., & Lazarian, A. 1999, ApJ, 512, 740
Draine, B. T., & Li, A. 2007, ApJ, 657, 810
Duncan, A. R., Haynes, R. F., Jones, K. L., & Stewart, R. T. 1995, MNRAS, 277, 36
Dunkley, J., Bucher, M., Ferreira, P. G., Moodley, K., & Skordis, C. 2005, MNRAS, 356, 925
Eriksen, H. K., et al. 2006, ApJ, 641, 665
Eriksen, H. K., et al. 2007, ApJ, 656, 641
Finkbeiner, D. P., Davis, M., & Schlegel, D. J. 1999, ApJ, 524, 867
Gelfand, A. E., & Smith, A. F. M. 1990, J. Am. Stat. Assoc., 85, 398
Geweke, J., & Tanizaki, H. 2001, Comput. Stat. Data Anal., 37, 151
Gold, B., et al. 2009, ApJS, 180, 265
Gorski, K. M., Hivon, E., Banday, A. J., Wandelt, B. D., Hansen, F. K., Reinecke, M., & Bartlemann, M. 2005, ApJ, 622, 759
Han, J.-L. 2006, Chinese J. Astron. Astrophys. Suppl., 6, 211
Heiles, C. 2000, AJ, 119, 923
Hildebrand, R. H., & Dragovan, M. 1995, ApJ, 450, 663
Hinshaw, G., et al. 2007, ApJS, 170, 288
Hinshaw, G., et al. 2009, ApJS, 180, 225
Jarosik, N., et al. 2007, ApJS, 170, 263
Jeffreys, H. 1961, Theory of Probability (3rd ed.; Oxford: Clarendon Press)
Kamionkowski, M., Kosowsky, A., & Stebbins, A. 1997, Phys. Rev. D, 55, 7368
Knox, L., Christensen, N., & Skordis, C. 2001, ApJ, 563, L95
Kogut, A., et al. 2007, ApJ, 665, 355
Lawson, K. D., Mayer, C. J., Osborne, J. L., & Parkinson, M. L. 1987, MNRAS, 225, 307
Lewis, A., & Bridle, S. 2002, Phys. Rev. D, 66, 103511
Miville-Deschenes, M., Ysard, N., Lavabre, A., Ponthieu, N., Macias-Perez, J. F., Aumont, J., & Bernard, J. P. 2008, A&A, 490, 1093
Nolta, M. R., et al. 2009, ApJS, 180, 296
Page, L., et al. 2007, ApJS, 170, 335
Reich, P., & Reich, W. 1988, A&AS, 74, 7
Rybicki, G. B., & Lightman, A. 1979, Radiative Processes in Astrophysics (New York: Wiley & Sons)
Seljak, U. 1997, ApJ, 482, 6
Spergel, D. N., et al. 2007, ApJS, 170, 377
Spitzer, L. 1998, in Physical Processes in the Interstellar Medium, ed. L. Spitzer (New York: Wiley), 335
Strong, A. W., Moskalenko, I. V., & Ptuskin, V. S. 2007, Annu. Rev. Nucl. Part. Sci., 57, 285
Strong, A. W., Moskalenko, I. V., & Reimer, O. 2000, ApJ, 537, 763
Uyaniker, B., Fürst, E., Reich, W., Reich, P., & Wielebinski, R. 1999, A&AS, 138, 31
Vallée, J. P. 2005, ApJ, 619, 297
Wandelt, B. D., Larson, D. L., & Lakshminarayanan, A. 2004, Phys. Rev. D, 70, 083511
Wolleben, M., Landecker, T. L., Reich, W., & Wielebinski, R. 2006, A&A, 448, 411
Zaldarriaga, M., & Seljak, U. 1997, Phys. Rev. D, 55, 1830